Systematic and quantitative structure-property relationships of polymeric medical nanomaterials: From systematic synthesis and characterization to computer modeling and nano-bio interaction and toxicity

Kegang Liu,[1,‡,*] Xueya Wang,[1,‡] Xiaochun Li-Blatter,[2] Marc Wolf, [1] Patrick Hunziker[1,3,4,*]

[1]Nanomedicine Research Lab. CLINAM, University of Basel, University Hospital Basel, Bernoullistrasse 20, CH-4056 Basel, Switzerland

[2]Biozentrum, University of Basel, Klingelbergstrasse 70, 4056 Basel, Switzerland

[3]Intensive Care Clinic, University Hospital Basel, Petersgraben 4, 4031 Basel, Switzerland

[4]CLINAM Foundation for Nanomedicine, Alemannengasse, 4058 Basel, Switzerland

[‡] These authors contributed equally to the work.

[*]Correspondence and requests for materials should be addressed to Dr. Kegang Liu, kegang.liu@unibas.ch; Prof. Patrick Hunziker hunzikerp@swissnano.org

ABSTRACT

Nanomaterials allow designing novel targeted therapies, facilitate molecular diagnostics and are therefore enabling platforms for Personalized Medicine. A systematic science and a predictive understanding of molecular/supramolecular structure relationships and of nanoparticle structure/biological property relationships are needed for rational design and clinical progress but are hampered by the anecdotal nature, nonsystematic and non-representative nanomaterial assortment and the oligo-disciplinary approach of many publications.

Here, we find that a systematic and comprehensive multidisciplinary approach to production, exploration of molecular-structure/ nanostructure relationship and nano-bio structure/function relationship of medical nanomaterials can be achieved by combining systematic chemical synthesis, thorough physicochemical analysis, computer modeling and biological experiments, as

shown in a nanomaterial family of amphiphilic, micelle-forming oxazoline/siloxane block copolymers suited for clinical application. This comprehensive interdisciplinary approach leads to improved understanding of nanomaterial structure, allows new insights into binding modes for the nanomaterial protein corona, induces the design of minimally cell-binding materials, and yields rational strategies to avoid toxicity. Thus, this work contributes to a systematic and scientific basis for rational design of medical nanomaterials.

KEYWORDS: PDMS-PMOXA polymer, self-assembling nanoparticle, computer modeling, structure-property relationship, nano-bio interaction

Nanomaterials are highly promising new materials for medicine because they can achieve, in a single particle, one or multiple desirable effects like delivery of poorly soluble drugs,[1, 2] control of drug biodistribution to certain tissues or diseases like cancer and inflammation by selective extravasation,[3] receptor-specific targeting,[4] delivery of diagnostic agents for molecular imaging,[5] triggered functionality, e.g. phototriggered cytotoxicity,[6] combined diagnostic and therapeutic features in "theranostic" particles.[7] They also allow to build nanosized objects with complex functionality, like artificial organelles targeted to specific cells.[8] In comparison to small molecular pharmaceuticals and biologicals, the production, characterization, pharmacological properties, mechanisms of biological interactions and in particular the mechanisms causing undesired and toxic effects are markedly different.[9, 10] While numerous publications about nanoparticles for medicine can be found in the recent literature, many of them are limited[11] by anecdotal nature, nonsystematic material assortment dictated by commercial availability rather than systematic design, choice of nanomaterials with the low potential for clinical application (e.g., solid polymer beads or hard metal nanoparticles), and by a mono- or oligo-disciplinary approach.

Nonspecific binding of plasma proteins like albumin or complement factors to nanoparticles ("corona formation"),[12-16] induction of and binding to preformed IgM,[17, 18] and nonspecific binding of nanoparticles to cells are well known,[19-21] and such nano-bio interactions are believed to be fundamentally influenced by surface properties at the molecular level and the nanoscale level. Surface properties may include molecular polymer structure, presence and distribution of hydrophobic domains[22] and charged residues[23] in the surface layer, formation of secondary or

tertiary structure by the polymer (as shown for PEG[24]) and nanoscale topology of the nanoparticle surface.[25]

Such effects at the molecular and nanoscale level are thought to be the key drivers of relevant macro-scale and clinical effects seen in patients. For example, premature removal of particles from the circulation due to shortened half-life, binding to non-targeted cells, uptake by the phagocyte system in liver and spleen,[26] systemic infusion reactions,[27] induction of PEG antibodies,[28] alteration of the "enhanced permeability and retention" (EPR) characteristics,[29] stimulation of immune cells[30] and interaction with the coagulation system.[31] When the upcoming paradigm of active nanoparticle targeting is considered where ligands on nanoparticles have to bind selectively to target receptors on target cells,[32-37] mechanistic understanding of binding versus stealth becomes even more important for rational design.

Specific nanomaterial properties might also determine elimination pathways as well as toxicity at short and long term. Limited knowledge about such key aspects may contribute to the observation that only few new nanomaterials have achieved clinical translation.

Thus, there is broad recognition that a more solid scientific, systematic and quantitative approach to medical nanomaterials is needed, ultimately promising a mechanistic framework and a predictive understanding that can lead to rational design strategies for medical diagnostics and therapeutics. For such a scientific framework for future nanomaterials, it is important to understand the impact of the chemical structure of the molecular building blocks on nanoparticle structure after self-assembly in a physiologic environment (*molecular structure/nanostructure relationship*) that ultimately might determine the nano-bio interaction of such particles (*nano-bio structure/ function relationship*).

To contribute to the scientific basis of medical nanomaterials, we use here a *constructive*, *mechanistic*, *quantitative* and *interdisciplinary* approach to study molecular-structure/nanostructure relationship and nano-bio structure/function relationship. This is achieved by systematic chemical synthesis, by thorough physicochemical analysis, by nanoparticle computer modeling, and by biologic experiments and is applied to a representative family of medical nanomaterials, namely the amphiphilic, micelle- and vesicle forming oxazoline/siloxane block copolymer nanomaterials

RESULT AND DISCUSSION

Polymers

As a prototypical amphiphilic polymer family for nanomaterial assembly, we chose the oxazoline/siloxane block-copolymer family (PMOXA-*b*-PDMS-*b*-PMOXA) because it is a proven platform yielding various functional nanomaterials;[38, 39] its hydrophilic oxazoline blocks are characterized by strong hydrophilicity (more so than PEG), excellent stealth properties,[40, 41] ease of controlled synthesis and accessibility to various chemical functionalization.[42,43] PDMS is well suited as a hydrophobic building block because these siloxanes are highly hydrophobic, chemically inert and biocompatible, and the PDMS segments are, as members of the silicone oil family, liquid at room- and body temperature, thus facilitating mechanistic understanding.[44] Nine series of amphiphilic copolymers were designed and synthesized by varying charges, functional groups, and the length ratio between PDMS and PMOXA segments (Figures 1a, 1b, and Table S1).

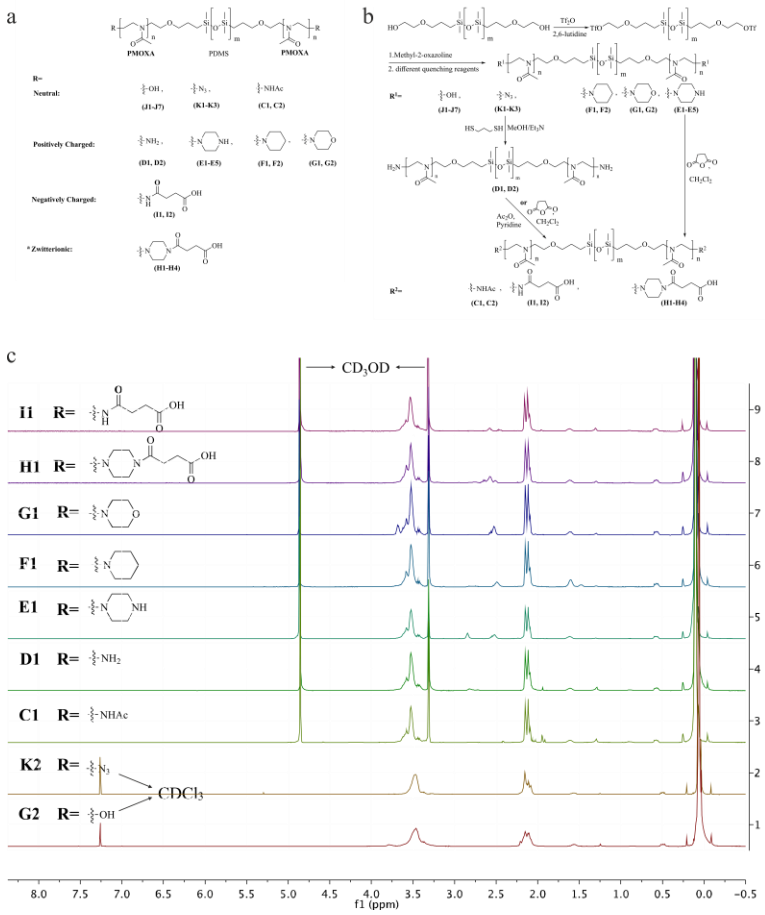

Figure 1. Polymer chemistry. (a) Structures of investigated polymers. Tri-coblock ABA PMOXA-b-PDMS-b-PMOXA with different termini (neutral, positively charged, negatively charged, and zwitterionic). [a] Since the H group based micelles show negatively charged surfaces

(Table S3), the H group is also assigned as a negatively charged group, see context below. (b) Schematic synthesis of tri-coblock ABA PMOXA-b-PDMS-b-PMOXA with different termini. (c) ^{1}HNMRs of representative examples of polymers (J2, K2, C, D1, E1, F1, G1, H1, I1). $CDCl_3$ as solvent for K2 and G2; CD_3OD as solvent for the rest of the compounds.

The 2-methyl-2-oxazoline was polymerized using the living cationic polymerization of the hydrophilic block (PMOXA) onto the hydrophobic block alpha-/omega-dicarbinol polydimethylsiloxane (PDMS, 73 siloxane units) that had been activated with triflic anhydride to serve as macro-initiator as shown in Figure 1b. The length of the hydrophilic PMOXA segments is determined by reaction time and monomer availability and was controlled by time dependent quenching. Nucleophilic termination was done with hydroxide, sodium azide, piperazine, piperidine, and morpholine, yielding copolymers series J, K, E, F, G, respectively; the copolymers C, D, H, I were then obtained through derivatization (Figure 1b). Copolymers series C, D, H, I were produced by terminal functional transformation; for example, reduction of polymer K under mild conditions (dithiol in basic conditions) resulted into polymers D, which were then acetylated to provide polymers C. Copolymers D and E reacted with succinic anhydride to produce copolymers H and I.

All the copolymers were well characterized in ^{1}HNMR. Length ratio of PDMS and PMOXA were determined as ranging from 18.3:1 (73 siloxane: 4 oxazoline) to 2:1 (73 siloxane: 37 oxazoline) by ^{1}HNMR. In representative ^{1}HNMR spectra in Figure 1c, the peak at around 0 ppm corresponds to the PDMS segment and peaks at around 2.0 ppm and 3.5ppm originate from PMOXA. Terminal groups can also be accurately distinguished (Figure 1c and Table S2). The 29 copolymers of the 9 series can be classified as 4 categories according to terminal group charge (Figure 1a and Table S1): neutral J, K, C; positively charged D, E, F, G; negatively charged I, zwitterionic H. Since the H group based micelles show negatively charged surfaces (Table S3), the H group can also be assigned as a negatively charged group, see with later context. The synthetic ease and the resulting purity of the products underscore the utility of oxazoline based polymers as a platform for systematic investigations and reproducible synthesis.

Molecule-Structure/Nanostructure Relationship

Self-assembly was induced by transferring the polymeric material to an aqueous, physiologic environment by microfluidic[45] and batch methods (see methods section). In transmission electron microscopy (TEM), the resulting nanomaterials were imaged (Figure 2a) and micelle hydrophobic radius and hydrophilic/hydrophobic interface area were determined (CryoTEM, Figure S1). From hydrophobic core size density and monomer count of PDMS, the hydrophobic block count per micelle (association number, Figures 2b and 2c), allows to determine the stoichiometry of block copolymer chains per nanoparticle as starting condition for computer modeling. Multiscale modeling of polymeric micelles started from known data from literature that was integrated in our molecular mechanics framework (see Supplementary information). Polyethyloxazoline (PEOXA) polymers are known from molecular dynamics studies to assume random coil configuration in the well hydrated state due to hydration enthalpy gains,[46] in contrast to the reported formation of helices in PEG[47] which is less hydrophilic and in PEI due to formation of intra-/inter-chain hydrogen bridges.[48, 49] PMOXA is even more hydrophilic than PEOXA and can be regarded as a prototypical well-hydrated polymer. Molecular mechanics optimization of short PMOXA segments was performed using the MMFF94s force field in the Avogadro software[50], yielding consistently preferred rotamer conformations of ± 90° at the backbone CN bonds and a predominance of trans versus gauche configuration at the backbone CC bond. These findings correspond well to molecular dynamics results of hydrated polyethyloxazolines. Using rotamer configurations in the proportions found in Ref.46 with an added noise term, large numbers of randomly varying copolymer structures were created and assembled to composite nanostructures in a self-assembly-like process as guided by the experimental findings in TEM. Figures 2a and 2b (TEM/modeling) give an overview over nanoparticle sizes determined using multiple methods and resulting in a series of models. Modeling shows that the hydrophobic blocks are in mushroom configuration (Figure 2b) rather than brush conformation and exposes the possibility that there are potential gaps between the hydrophilic strands that are large enough to expose the hydrophobic surface to molecules from the outside and suggests one possible mechanism for nonspecific binding.

Note that with increasing block size of the hydrophilic segment (same hydrophobic segment), the size of hydrophobic part decreases, but surface area per monomer increases (Figure 2c) the peak for hydrophilic monomer density per volume is approximately constant while the peak location moves outward from the interface (Figure 2d) – these parameters are therefore potential

candidates for rational design. For details see supplementary information (*Self-assembly in aqueous solution: from polymer structure to micelle shape elucidated by computer modeling*).

a

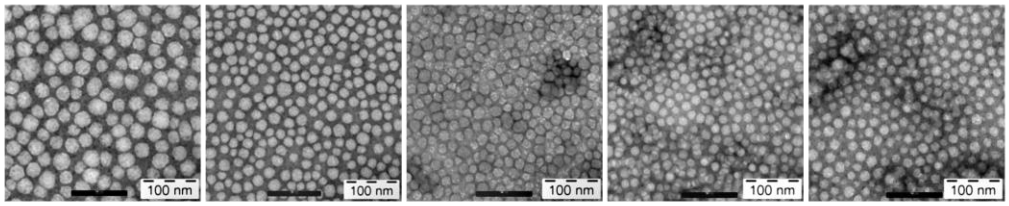

J2 -OH-7 B_{73}-(A_7-$OH)_2$ | **J4** -OH-12 B_{73}-(A_{12}-$OH)_2$ | **J5** -OH-17 B_{73}-(A_{17}-$OH)_2$ | **J6** -OH-19 B_{73}-(A_{19}-$OH)_2$ | **J7** -OH-37 B_{73}-(A_{37}-$OH)_2$

b

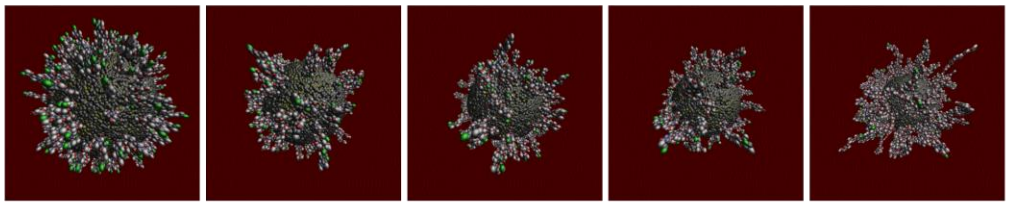

B_{73}-(A_7-R)$_2$ | B_{73}-(A_{12}-R)$_2$ | B_{73}-(A_{17}-R)$_2$ | B_{73}-(A_{19}-R)$_2$ | B_{73}-(A_{37}-R)$_2$

c

No	Ø (nm)	ABA Abbreviation in Formula[a]	Num. of monomers per micelle (Median)	Surface area per monomer (Median)
J2	33.7 ±1.2	**B_{73}-(A_7-R)$_2$**	**742.1355**	2.3633
J4	28.0 ±2.6	**B_{73}-(A_{12}-R)$_2$**	**258.3594**	3.3595
J5	29.6 ±2.5	**B_{73}-(A_{17}-R)$_2$**	**206.4309**	3.6204
J6	29.1 ±2.4	**B_{73}-(A_{19}-R)$_2$**	**150.7781**	4.0201
J7	24.9 ±5.0	**B_{73}-(A_{37}-R)$_2$**	**138.9012**	4.1316

d

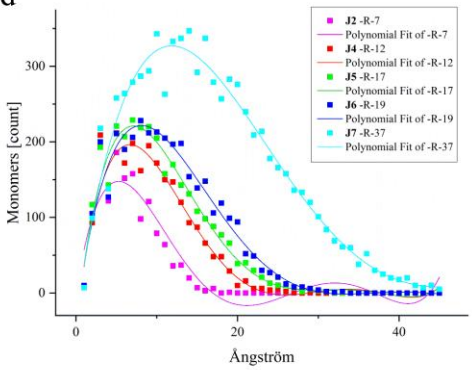

Figure 2. Impact of polymer structure on morphology. (a) TEMs of polymeric micelles derived from triblock copolymers **J** B_{73}-(A_m-$OH)_2$ with increasing PMOXA lengths, m= 7, 12, 17, 19, 37. (b) Simulated micelles with fixed PDMS length and variable PMOXA lengths (7, 12, 17, 19, 37). PDMS hydrophobic core: black grey; PMOXA hydrophilic strand: green-T (terminus); white-methyl; blue-N and red-O. (c) Number of monomers per micelle from calculation and surface area per monomer (Median**)** [a]Polymer ABA can be represented by an abbreviated formula **B_n-(A_m-R)$_2$** or even a shorter abbreviation**:-R-m** (see Figures 2a, 2d and Table S3). Hereinto, A: PMOXA block; m: length of PMOXA; B: PDMS block; n: length of PDMS; R: an abbreviation of a terminal function group. d) Monomer distribution on micelle surface as from molecular simulation.

Nano-Bio Interaction (Cellular Uptake)

Physicochemical properties of nanocarriers such as size,[51, 52] shape,[51] surface charge[53, 54] and hydration shell,[55] are known factors modulating bio-nano interaction including cellular binding, uptake, protein surface binding,[13-16] and toxicity. To investigate cell interactions of polymeric micelles, hydrophobically modified Rhodamine B dye was encapsulated by co-precipitation during self-assembly. The cellular uptake of the micelle into the HeLa cell line was assessed by flow cytometry. In addition to physicochemical characterization and biological experiments, the use of computer modeling of the nanomaterials via a multiscale approach contributed insights to nanoparticle structure and enabled an enhanced mechanistic understanding of the relationship between polymer chemistry, nanosystem structure, and biological effects. Non-specific cell binding and uptake was affected by hydrophilic block length and terminal group: polymers with positive charge but short hydrophilic blocks exhibited high non-specific cell binding (Figure 3), while an increase in hydrophilic block length reduced the impact of terminus charge, understood as a reduced availability of charges in the outer micelle layer (Figure 4a) as predicted by modeling results showing a random coil structure in aqueous solution of this polymer (Figure 4b). Observational studies have reported that surface charges of nanoparticles are important for nano-bio interactions.[56-58] We therefore investigated the structure-function relationship of charged groups, charge parameters, and cell interaction in more detail using the synthetic and modeling information. Charges may be imparted to a polymer surface in the presence of charged groups, through binding, e.g. amide complexation of ions formed, or through surface effects mediated in yet different ways.[59]

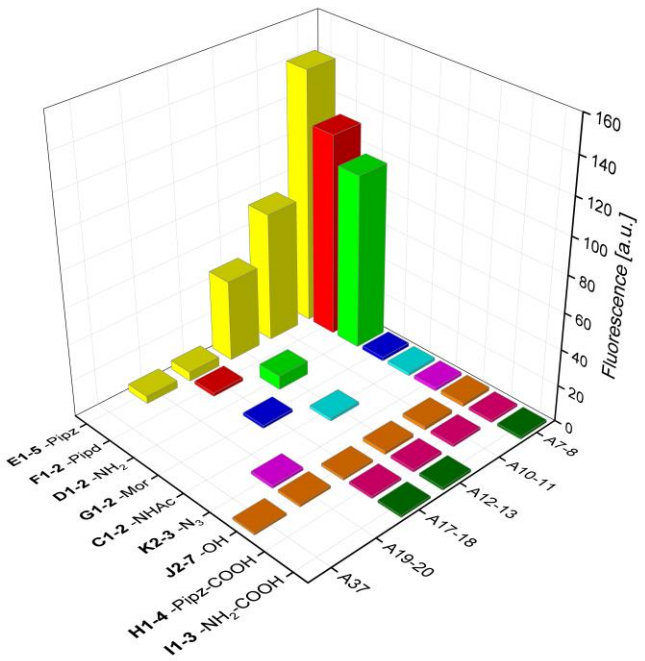

Figure 3. Cellular uptake in HeLa cells of fluorescently labeled tri-block amphiphilic polymer with different termini R and PMOXA lengths Am after 8 h incubation as investigated by flow cytometry**.**

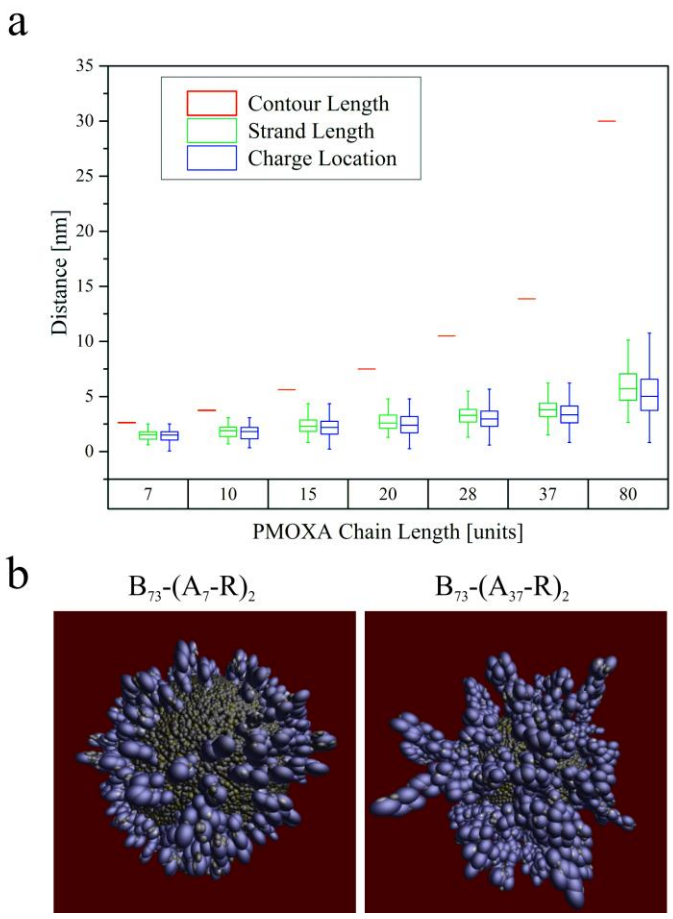

Figure 4. (a) Graph showing the hydrophilic strand protrusion from the hydrophobic shell and the charge of the outermost polymer residues for various polymer types. A smaller distance difference between the strand length and charge location shows a higher density of the surface charge. b) Simulated micelle (hydrated) B_{73}-(A_7-R)$_2$ (left) and micelle B_{73}-(A_{37}-R)$_2$ (right). PDMS hydrophobic core: black grey; PMOXA hydrophilic strand: blue.

Zeta potential determination is a frequently used method to determine global surface charges of nanomaterials and relies on the mobility of charges in different layers in proximity to the particle.[60] As the electrostatic interaction between charged residues in physiologic buffers is a local phenomenon with an electrostatic screening length (Debye length) of less than 1 nm, we felt that beyond Zeta potential measurement, geometric charge distribution in 3D could be an additional key to understanding the impact of charges on nano-bio interactions.

Modeling of the charge distribution in hydrophilic polymer surface with charged terminal shows its proximity to particle's outermost layer (Figure 4a), resulting in a highly planar and strongly charged layer, a high absolute value of the zeta potential (Table S3), and in case of positive

charges, strong nonspecific binding to cells. The surface charge distributions of E4 B_{73}-(A_{17}-Pipz)$_2$ and E1 B_{73}-(A_7-Pipz)$_2$ based micelles were also proved through electrokinetic charge calculation based upon their zeta potentials (See supplementary information).

Charge distribution modeled in micelles with long hydrophilic blocks revealed that a significant proportion of charged groups is now buried within the thick hydrophilic layer and is located farther away from the shell than the Debye length (2 nm) from the outermost layer of the particle. A participation of those charges in nano-bio interactions is not expected. Also, the surface "roughness" in the latter particles is larger due to the alternative occurrence of protruding and folded strands, potentially reducing the accessibility of charged groups. While positive charge favors cell-binding of nanomaterials, as documented in the literature and found in our results, we observed experimentally a strongly diminished nonspecific cell binding with positively charged polymers when the hydrophilic blocks are long enough (Figure 3), as predicted by the modeling. This was accompanied by some decrease of the Zeta potential; but the Zeta potential alone did not fully explain the amount of nonspecific cell binding. Notably, negatively charged termini, specific end groups consisting of a positive charge embedded in a larger group (N-morpholine terminus with a pKa ~8, Table S2) and zwitterionic species (family H) showed low cell binding. Thus, we believe that charge distribution modeling plays an important role in the rational design of polymeric nanosystems for medicine.

Neutral polymers showed low binding with marginal impact of block length and negatively charged polymers had the lowest binding (Figure 3). Cell uptake (micelles with positively charged surface) was temperature dependent and thus active (Figure 5) (See supplementary information for details). The cytotoxicity of all studied polymer based micelles was low (Figure 6).

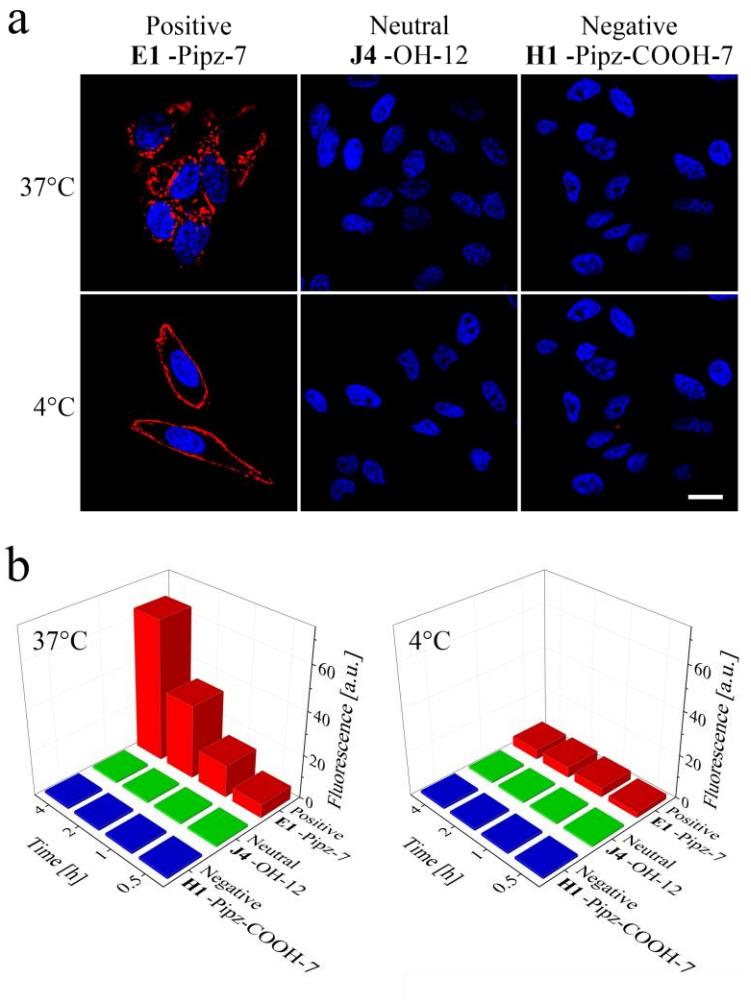

Figure 5. Cellular uptake in HeLa cells of fluorescently labeled tri-block amphiphilic polymer at 4°C and at 37°C. a) Representative laser scanning confocal microscopy images of HeLa cells incubated with polymers E1 (-Pipz-7), J4 (-OH-12), H1 (-Pipz-COOH-7) at 4°C and 37°C after 4h incubation. All bars indicate 10 μm. b) HeLa cells were incubated with polymers for 0.5, 1.0, 2.0 and 4.0 h and investigated by flow cytometry.

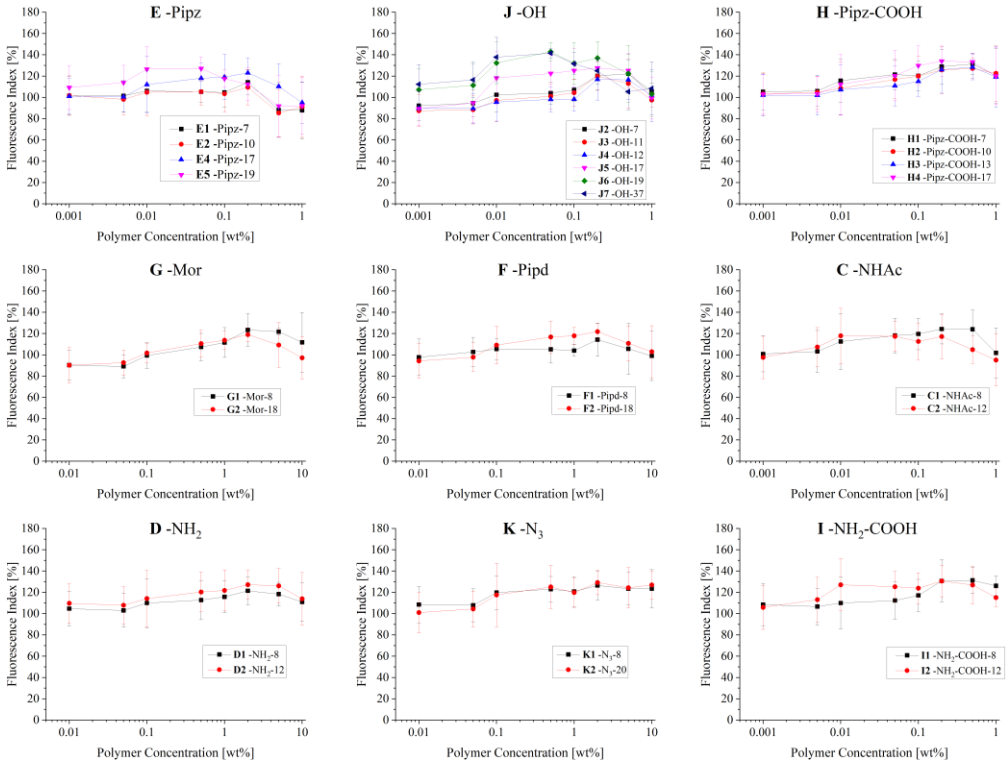

Figure 6. Cell viability of tri-block amphiphilic polymer in HeLa cells as determined by cell proliferation assay after 24 h incubation. Experiments were performed in quadruplicate and data is expressed as means ± standard deviation (SD).

The reported methods and results contribute to a knowledge-based and predictive science for the design of future polymeric nanosystems for medical applications.

This approach leads to lessons towards rational design of such materials, indicates potential binding models for the nanomaterial protein corona, induces the design of minimally cell-binding materials, and yields strategies to prevent nanomaterial toxicity. Thus, this work contributes to a systematic and scientific basis for a rational design of medical nanomaterials.

Nano-Bio Interaction (Effect of Chemistry and Shape on Plasma Protein Binding and Complement Activation)

A proper understanding of the interaction of plasma proteins with nanoparticles is of great importance for their successful application in nanomedicine.[13-16] Due to the interactions between nanoparticles and proteins, the conformation of proteins may alter and novel epitopes may be exposed to their surface leading to unexpected biological reactions and toxicity. Human serum albumin (HSA), the most abundant protein in plasma (4-5% w/v) regulates osmotic pressure and

transport and metabolism of numerous compounds in the organism (e.g., fatty acids, drugs, hormones, metal ions). Hereby, we arranged a systematic assessment of the absorption of HSA and analogous bovine serum albumin (BSA) at various copolymers based nanoparticles through measurements of the changes of their sizes (Z-average hydrodynamic diameter), surface charges (ζ-potential) and dissociation constants (K_D). Here, six groups of polymeric micelles with 2 different PMOXA lengths (7 and 17 MOXA units) and 3 different terminal groups (-Pipz, -OH, -Pipz-COOH) were chosen for further measurements, respectively, i.e. **E1** -Pipz-7, **E4** -Pipz-17; **J2** -OH-7, **J5** -OH-17; **H1** Pipz-COOH-7, **H4** -Pipz-COOH-17. Figure 7a shows the influence of the length and terminal groups of copolymers on sizes and surface charges of these copolymers based micelles with a titration of HSA. Figures 7a-A and 7a-C show that Z-average diameters of micelles increased upon binding. The polymeric micelles have similar sizes (30-37 nm) in the absence of HSA and the increase of the sizes upon terminal group follows the order: -Pipz > -OH > -Pipz-COOH. On the other hand, micelles constructed by the longer length of PMOXA (17 MOXA) are smaller than the one with the shorter length, except micelles with zwitterionic group (-Pipz-COOH) modified surfaces. This observation is consistent with the change of related ζ-potential of micelles during the titration. Fig 7a-B shows the ζ-potential of polymeric micelles upon binding with the titration of HSA, which is the surface potential measured at a distance of about 0.2 nm away from the plane of micelles with HSA binding.

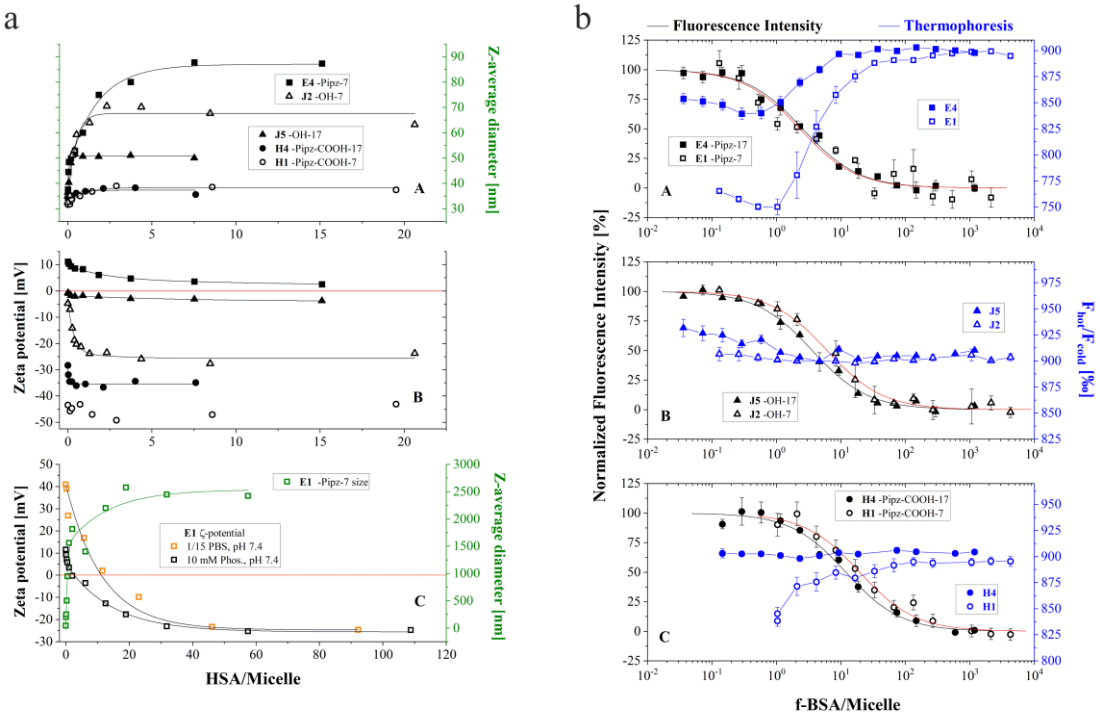

Figure 7. (a) Monitoring of the changes of size and zeta-potential of the polymer based micelles upon HSA absorption (titration). A and B: Z-average hydrodynamic diameters (plot A) and zeta potentials (plot B) of polymer micelles (E4; J2, J5; H1, H4) as a function of HSA concentration. C: zeta potential and Z-average hydrodynamic diameter of **E1** based micelles as a function of HSA concentration. (**b)** Interactions of f-BSA with different polymer based micelles monitored by both fluorescence intensity (FLI) and microscale thermophoresis (MST). The concentrations of f-BSA (50nM or 100 nM) were kept constant during the measurements, while mixing them with increasing concentrations of polymers. Normalized fluorescence intensities of f-BSA as a function of polymer concentration are presented (black symbols), data fitted with 1:1 binding model (black lines for **E4**, **J5** and **H4**; red lines for **E1**, **J2** and **H1**); changes of hot/cold signal of f-BSA upon binding were also recorded (blue). A: **E1**, **E4**; B: **J2**, **J5**; C: **H1**, **H4**.

For micelles with neutral surfaces, the size of **J2** -OH-7 based micelle after saturation with HSA went up to 70.4 nm and the ζ-potential increased from around 0 to -22 mV (ζ-potential of HSA alone in solution), which demonstrates that HSA was just adsorbed to the outer layer of the micelles. Less change was observed for **J5** -OH-17 based micelles. The increment of micelle diameter was 14 nm (twice the HSA molecular diameter) and the ζ-potential had a tiny decrease (to -3.1 mV). For micelles surfaces modified with zwitterionic groups (in general, negatively charged, **H4** -Pipz-COOH-17 and **H1** -Pipz-COOH-7), the variation of size (diameter increased around 5-7 nm) and ζ-potential (decreased around 5 mV) is less in dependent upon the change of polymer chain length. In contrast to micelles with neutral and negative surfaces, the positively charged micelles displayed huge variations in sizes. The diameter of copolymer **E4** -Pipz-17 based micelles increased to 87.8 nm after HSA saturation and ζ-potential decreased from 9.1 to 2.1 mV. In addition, Fig 7a-C demonstrates the dramatic changes of the size and ζ-potential of **E1** -Pipz-7 based micelles. The size of micelles rapidly went up, whereas the positive charge of -Pipz-7 was neutralized by HSA at a concentration of 0.5 μM (d_H = 1750 nm). Further titration of HSA led to continuous increase of size up to 2000-3000 nm and the ζ-potential dropped to -20.5 mV and concurrently the solution became turbid at the end of the titration, and precipitation was observed thereafter.

From the above phenomena, the interaction between HSA and polymeric micelles is highly dependent on the terminal charge and hydrophilic length (PMOXA) of copolymer. Therefore,

hydrophobic interaction, electrostatic interaction, even hydrogen bonds play a role in the binding processes. According to above TEMs and computer modeling, micelles with longer length of PMOXA (17 MOXA units) show a more flexible outer layer, lower charge density and less hydrophobic space as compared to the micelles with shorter of PMOXA (7 MOXA units). Hydrophobic interaction or hydrogen bonding plays a prominent role in the interaction between the HSA and micelle. Presumably, HSA may be embedded in the hydrophilic outer layer. Of course, charge also influences this tendency. Micelles with positively charged surfaces showed large size effects as shown in Figure 8b and negatively charged showed small size effects, both of which are due to charge attraction and repulsion, respectively. For the micelles with short PMOXA lengths, both hydrophobic and electrostatic interactions have a synergistic effect on the size increase for micelles with positively charged surface. Here, negatively charged HSA works as a crosslinker to bind these micelles as shown in Figure 8a. **J2** -OH-7 (neutral) based micelles may only have relatively strong hydrophobic interaction with HSA. Similar to micelles with negatively charged surface (long PMOXA chain), **H1** -Pipz-COOH-7 based micelles have strong charge repulsion with negatively charged HSA, thereby preventing size increase. On the other hand, hydrophobic interaction and possible tiny charge attraction with the residual positive charge of HSA may contribute to the small size increase.

For a further elucidation of the interactions between proteins and polymeric micelles, we used fluorescence labeled BSA (f-BSA) as an analogue of HAS and titrated with three types of polymeric micelles using fluorescence and thermophoresis techniques. The measured K_D is listed in Table S4. The binding stoichiometry could not be determined accurately from these measurements, even though more than one polymer binding to HSA was observed by several techniques (DLS, ζ-potential, FLI). For this study, a 1:1 binding model was assumed. As shown in Figure 7b, micelles with longer length of PMOXA (17) showed higher binding affinity of HSA than micelles with shorter PMOXA (7). This further proves that micelles with shorter PMOXA have a relatively rigid outer layer, which impedes further tight hydrophobic and electrostatic interactions with f-BSA. The thermophoresis of the binding studies showed the evident changes with **E1** -Pipz-7 based micelles, which can be explained by a larger change of charge and entropy of the hydration shell of f-BSA.[61] In contrast, there is no significant change of thermophoresis upon f-BSA binding to the remaining polymeric micelles (Figure 7b). In addition to thermophoresis, the secondary structure of HSA in the presence of 3 different polymer micelles was determined by CD spectroscopy. The analysis of HSA in buffer (10 mM phosphate, pH 7.4)

was assessed as 54.5±2.2% α-helix, 5.4±2.1% β-sheet, 36.2±3.5% random coil, and 6.4±1.6% β-turn. There were no significant changes of secondary structure upon binding with polymeric micelles (Figure S3).

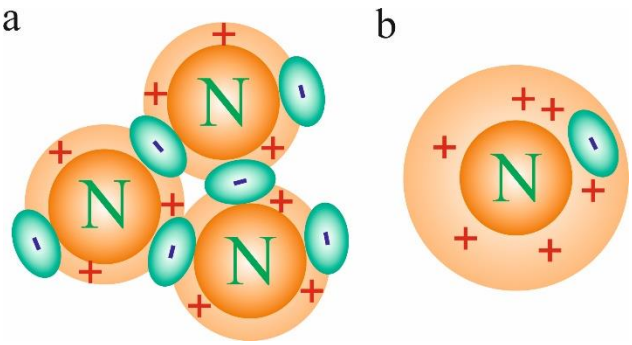

Figure 8. Cartoon showing an interaction between the positively surface charged nanocarrier constructed with different length of PMOXA segment and HSA: (a) Negatively charged HSA works as a crosslinker to bind these micelles built by the polymer with a shorter PMOXA length (E1); (b) Micelles with positively charged surface shows a large size and may partially encapsulate the HSA molecules.

Nano-bio interaction (in vivo)

Based on the above studies, we further evaluated the influence of the charge and length of the polymers PMOXA-PDMS-PMOXA *in vivo*. First, three types of polymers **J2** -OH-7, **E1** -Pipz-7 and **H1** -Pipz-COOH-7 were selected with the same PMOXA length 7 and different termini: neutral -OH, positively charged -Pipz, negatively charged -Pipz-COOH, respectively. The nanomaterials based on the above polymers were administrated to male C57BL/6 mice *via* intra-venous injection. Tissue distribution analysis upon sacrificing of the mice after one week was conducted, where we found strong fluorescence signals in the liver and lymph nodes for **H1** polymers, but not for **J2** and **E1** polymers (Figures 9a and S4). This indicates that negatively charged surfaces of the nanomaterials promoted a long lifetime in blood circulation and a great consistency of the relationship between the surface charge and unspecific cellular uptake of the nanomaterials as studied above. In a word, first, a strong unspecific cellular uptake of nanomaterials entailed fast metabolism and clearance from the body of the mice. Second, similar experiments using different lengths of PMOXA (7 and 17) and the same charged terminus (-Pipz-COOH) of nanomaterials (**H1** and **H4**) further demonstrated that the micelles with a short PMOXA length and negatively charged surface have strong charge repulsion with negatively

charged cell membrane surfaces in the organs, resulting in a long lifetime within the body of the mice (Figure 9b). Third, elimination of nanoparticles via feces confirmed the above results (Figure 9e). Due to the specific behavior of the **H1** based micelles in the above experiments, a full-time spectrum (24 h to 3 months) of the bio-distribution of the micelles in male C57BL/6 mice was conducted and the result is shown in Figure 9d, which indicates a long duration (>1 week) and a strong intensity of nanocarrier accumulation in lymph nodes. Presumably, **H1** based micelles can be utilized as a potential ideal nanocarrier candidate in the field of immune therapy. Furthermore, a targeted biodistribution using **H1** based micelles in NOD-SCID mice (subcutaneous xenograft of C8161 cells) was confirmed by a strong fluorescence signal in the tumor (Figure 9c). Therefore, the nanocarrier design and synthesis assisted by a computer modeling can accelerate the exploration of novel nanodrugs.

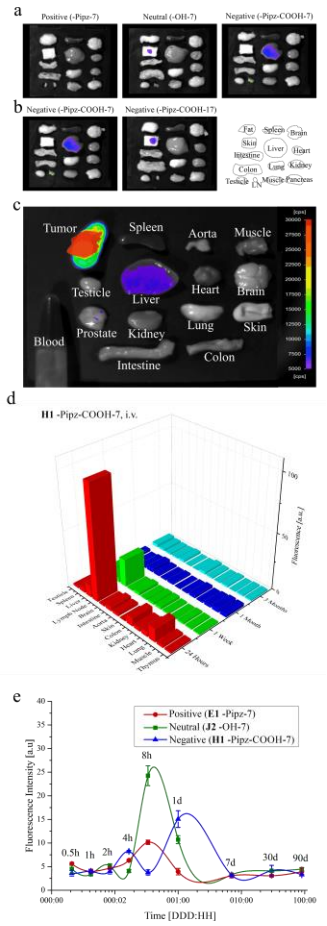

Figure 9. (a) Biodistribution (1 week after i.v. injection) of micelles built by copolymers having same length of PMOXA (7 units), but different terminal charge (Neutral -OH, positively charged -Pipz, and negatively charged -Pipz-COOH). (b) Biodistribution (1 week after i.v. injection) of micelles built by copolymers having different lengths of PMOXA (7, 17 units), but identical

terminus (-Pipz-COOH). (c) Binding assay *in vivo* – targeting of C8161 cells by the FA (folic acid) conjugated copolymer -OH-7 based micelles (organ dissection after 72 h). (d) Biodistribution of -Pipz-COOH-7 based micelles versus time in different organs of mice after i.v. injection. (e) Excretion of different terminal charged micelles in feces versus time after i.v. injection. Note: for fluorescence measurements Rhodamine B was covalently coupled to a hydrophobic polymer (PDMS) with a specific length to encapsulated well in PMOXA-PDMS based micelles.[45]

CONCLUSIONS

Well-characterized polymers were systematically synthesized with varying chain lengths and terminal groups, followed by nanosystem self-assembly, physicochemical characterization, and examination of nano-bio interactions, namely protein surface binding, cell binding, cellular uptake, cytotoxicity, and biodistribution. Computer modeling of the nanomaterials using a multiscale approach contributed insights to nanoparticle structure and enabled a mechanistic understanding of the relationship between polymer chemistry, nanosystem structure, and biological effects. Non-specific cell binding and uptake was affected by hydrophilic block length and terminal group: polymers with positively charged terminal but short hydrophilic blocks exhibited high non-specific cell binding, whereas an increase in hydrophilic block length reduced the cell binding. The impact of terminal charge, understood as a reduced availability of charges in the outer micelle layer was predicted by modeling results. The hydrophilic segment of these polymers shows a random coil structure in aqueous solution. Neutral polymers showed low binding with marginal impact of block length. Negatively charged polymers had the lowest cellular uptake. Cellular uptake was temperature dependent and thus active. Cytotoxicity was low. The reported methods and results contribute to a knowledge-based and predictive science for the design of future polymeric nanosystems for medical applications

MATERIALS AND METHODS

Materials. All substances for polymer synthesis were purchased from Sigma-Aldrich (St. Gallen, Switzerland) and ABCR (Karlsruhe, Germany) and were used as received unless otherwise stated. 2-methyl-2-oxazoline, chloroform and acetonitrile were dried by refluxing over CaH_2 under dry argon atmosphere and subsequent distillation prior to use. Bovine serum albumin (BSA) and human serum albumin (HSA, purity ≥ 99%) were purchased from Sigma Aldrich (Steinheim,

Germany). BSA was labelled with fluorescein (f-BSA, purity ≥ 99 %). The concentration of HSA was calculated by recording the UV absorption at 280 nm with an extinction coefficient of 35,700 $M^{-1}cm^{-1}$. Buffer: PBS solution and phosphate powder were obtained from Sigma-Aldrich; buffer (10 mM phosphate, pH 7.4), 1/10 PBS at pH 7.0 and pH 7.4, 1/15 PBS at pH 7.0 were made with nanopure water at a resistivity of 17 to 18 MΩ×cm, then filtered through a 0.2 μm regenerated cellulose filter (Infochroma AG, Zug, CH) before using.

^{1}HNMR measurement. The ^{1}H-NMR spectra were recorded with a Bruker DPX-400 spectrometer (Bruker, Switzerland). Deuterated chloroform (99.8% D) and Deuterated methanol (99.8%) were used as solvents. Spectra were analyzed with MestReNova 7.0.3 software (Mestrelab Research SL, Spain) and calibrated using solvent signals ($CDCl_3$, 7.26ppm; CD_3OD, 3.31ppm). The molecular weights of the polymers were obtained from ^{1}HNMR calculation.

Synthesis of ABA amphiphilic triblock PMOXA-b-PDMS-b-PMOXA copolymers. The polymerization and work-up procedures were synthesized and modified according to our previously described synthetic methods[45] and the procedures provided in the Supplementary Information.

Preparation of micelles. To prepare the micelles, 5 mg of polymer was dissolved in 20 μL of ethanol under stirring at room temperature. With this solution, 0.98 mL of phosphate-buffered saline (PBS, pH 7.4) was added dropwise. After 2 h of continuous stirring, the solution was filtrated through filters of defined pore size (Millex-GV, 0.22 μm; Millipore) to generate a homogenous population of micelles. To produce fluorescence-labeled polymer micelles, hydrophobically modified rhodamine B was used.

TEM and Cryo-TEM. The morphology of PMOXA-PDMS-PMOXA was characterized by TEM (JEM-1400, JEOL) after staining with 2% (w/v) uranyl acetate. The size distribution of PMOXA-PDMS-PMOXA was measured from the obtained TEM images with ImageJ.

Analysis of size and composition by electron microscopy. Polymeric micelles were analyzed by automated particle counting and quantification using the ImageJ package. For each polymer micelle type, several hundred micelles were detected, their cross-sectional area measured, and the

radius and hydrophobic volume computed. Based on the known specific weight of PDMS and the hydrophobic block length, the number of PDMS blocks per micelle, corresponding to the number of copolymer strands per micelle, was computed. From these measurements, surface area per hydrophilic block can be derived.

The hydrophilic shell is in a dehydrated state in TEM, but it is compatible to metal ions due to the carbonyl group, therefore, the minimal distance between two adjacent hydrophobic cores is a measure of the combined thicknesses of the dry shells including interspersed ions from the contrast agent (uranium acetate 2%). In high-resolution cryo-TEM, micelles are hydrated, and a rim compatible with the hydrophilic shell that can be measured is usually seen if image quality is excellent.

Modeling. Polymers and polymeric micelles were modeled using a multiscale strategy with the molecular modeling software „Computational Molecules" (http://www.computational.ch). A multiscale strategy was chosen because the large number of atoms per polymer strand (up to 1,500 atoms) and per micelle (up to 700,000 atoms) renders full ab initio modeling infeasible at this moment. PDMS blocks were likewise modeled in an atom-by-atom fashion based on known geometry of the PDMS backbone[50] and assuming random rotational of the SiO bond. Polymeric micelles were modeled by starting by construction of a hydrophobic sphere with the experimentally known diameter. Hydrophilic PMOXA segments were then grafted onto the hydrophobic shell at random locations on the shell with an inside-to-outside orientation, choosing the segment density per area known from experiments. Inter-strand interaction in the hydrophilic shell was not modeled due to the huge number of potential interactions.

Surface activity measurements (SAM). The measurements were performed with a Teflon trough (filling volume 3 ml) at ambient temperature in PBS buffer. The surface pressure, $\pi = \gamma_0 - \gamma$, where γ_0 is the surface tension of the pure buffer and γ the surface tension of the polymer solution, was monitored with filter paper (Whatman No. 1) connected to a Wilhelmy balance. Polymer solution (0.5 mg mL^{-1} or 0.1 mg mL^{-1}) was injected with a Hamilton syringe into the buffer subphase, which was stirred continuously by a magnetic stirring bar. From the π/logC plots of the polymers, the intersection of the 2 linear lines with different slopes is defined as the critical micelle concentration (CMC) of the polymer. The free energy of micelle formation,

ΔG^0_{mic}, calculated as $\Delta G^0_{mic} = RT \ln(CMC/C_w)$, where C_w is the molar concentration of water and corrects for the cratic contribution C_w = 55.5 mol/l at 24 ± 1°C [62].

Light Scattering and ζ-potential (ZP) measurements. The size and ZP of polymer micelles were performed on a Zetasizer Nano-ZS instrument (ZEN3600; Malvern Inst., Worcestershire, UK) in the presence of various HSA concentrations. The instrument is equipped with a 4 mW HeNe laser with a wavelength of 633 nm and with noninvasive 173° angle back scattering. The *z*-average size is intensity mean. All samples were filtered (0.2 μm) and degassed before using and the measurements were performed at 37 °C.

Fluorescence intensity (FLI) and microscale thermophoresis (MST) measurements. Binding of HSA to polymer micelles was studied by FLI and MST with f-BSA. The experiments were conducted in a Monolith NT.115T device using hydrophobic treated capillaries (NanoTemper Technologies). Signal Changes in FLI and MST due to binding were recorded with blue channel optics of the instrument (λ_{ex}= 470 ±15nm, λ_{em}=520 ±10nm), during a 30 s period of infrared laser heating at 50% of maximum laser power followed by a 5 s cooling period. Measurements were performed with PBS buffer. [61]

Circular Dichroism (CD) Measurements. CD spectra of HSA (1.89 μM) were measured in the absence and presence of polymer micelles (143 μM) in buffer (10 mM phosphate, pH 7.4) at 37 °C. The path length of the cuvette was 1 mm, and the bandwidth was adjusted to 1 nm. The samples were filtered (0.2 μm) and degassed before using. The percentage of protein secondary structure was estimated from a computer simulation based on a linear combination of α-helix, β-sheet, random coil, and β-turn reference spectra taken from ref. [63]

Cell culture. HeLa cells and C8131 cells were purchased from DSMZ and ATCC, respectively. The cells were adapted to grow in Roswell Park Memorial Institute 1640 Medium (RPMI 1640 Medium). All cells used in the experiments were cultured in RPMI 1640 medium containing 10% heat inactivated fetal calf serum (FCS), 1% GlutaMax™, 1% penicillin/streptomycin and 1% NEAA. Cultures were maintained at a temperature of 37°C in an atmosphere of 5% CO_2. All cell culture materials were obtained from Gibco Life Technologies, Inc. (Grand Island, NY). Cells were used 24 hours after seeded unless otherwise stated.

Cytotoxicity assay. HeLa cells were seeded in 96-well plates (1×10^4 cells / well / 100µL in full media) for 24 h before further treatment. Subsequently, the cells were incubated with micelle solutions at concentrations ranging from 0.01-10 mg mL^{-1}. After 24 h incubation, the cytotoxicity of each micelle was determined by CellTiter 96® AQ_{ueous} One Solution Cell Proliferation Assay (Promega). As negative control, wells which had no cells plated onto were used; for positive control, cells were incubated with media alone. All experiments were performed in triplicate and data presented in means ± standard deviation (SD).

Cellular uptake. The cellular uptake of fluorescently labeled polymers was performed using flow cytometry and laser scanning confocal microscopy. For the flow cytometry, HeLa cells were treated with micelle solutions at concentrations of 250 µg mL^{-1} for 0.5, 1, 2, 4 or 8 h. After washing twice with ice-cold PBS, cells were trypsinized and centrifuged. The pellet was resuspended in PBS containing 1% BSA at a concentration of 1×10^6 cells mL^{-1}. The micelle uptake was analyzed using a BD Accuri C6 flow cytometer (Becton Dickinson, San Jose, CA). For each quantitative analysis a cumulative number of 10^4 cells were collected in the live cell gate as defined by the typical pattern in the forward (FSC) and sideward scatter (SSC) display. The mean fluorescence intensity was analyzed using Flowjo® software. All experiments were performed three times and data presented in means ± standard error of the mean (SEM).
For the laser scanning confocal microscope studies, HeLa cells (2×10^4) were seeded onto 10 mm round glass coverslips placed in 24-well plates and grown overnight. Cells were treated with micelle solutions at concentrations of 250 µg mL^{-1} for 4 h. After washing twice with ice-cold PBS, the cells were fixed with 4% paraformaldehyde and nuclear stained with DAPI. Washed coverslips were placed onto glass microscope slides and the micelle uptake was visualized using a Laser scanning confocal microscope (Carl Zeiss LSM 710 Meta, Peabody, MA).

Animals. C57BL/6 and NOD/SCID gamma-c (NSG) mice (The Jackson Laboratory) were bred and maintained in the animal facility of the Department of Biomedicine of the University Hospital Basel under specific-pathogen-free conditions on a 12-hour day and 12-hour night schedule with *ad libitum* access to food and drinking water. Body weight and behavior of all mice in the experiments were monitored repeatedly over the exposition period.

Tissue distribution of nanoparticles. Male C57BL/6 mice, 6–8 weeks old, weighing between 20 and 25 g were selected and placed into different groups with three mice per group based on the particles they were treated with and the time frame of treatment. 50 mg kg^{-1} fluorescently labeled micelles in PBS were intravenously injected into mouse-tail vein. A control group of male C57BL/6 mice received the same volume of PBS. Full necropsies were conducted on the mice at 1 h, 2 h, 4 h, 8 h, 24 h, 1 week, 1 month and 3 months post intravenous injection. The heart, liver, spleen, lung, kidney, pancreas, small intestine, colon, testicle, lymph nodes, muscle, skin and fat were collected and subjected to fluorescence analysis to macroscopically detect the fluorescently labeled micelles with a NightOWL II device (Berthold Technologies, Bad Wildbad, Germany). In order to quantitatively analyze the organ fluorescence, the organs were fixed in 4% paraformaldehyde for 4 h and equilibrated in 30% sucrose–PBS (wt/vol) overnight at 4 °C, then detected with Synergy H1 (Hybrid Multi-Mode Reader, BioTek, Germany).

Elimination of nanoparticles. After i.v. injection of fluorescently labeled micelles into mouse tail vein, feces was collected at 0.5 h, 1 h, 2 h, 4 h, 8 h, 24 h, 1 week, 1 month and 3 months and dried over night at 40 °C, then stored at -20 °C for further analysis. Before analysis, feces was dried for 2 hours at 40 °C, weighed and dissolved in PBS. The fluorescence intensity of feces solution was detected with a Hybrid Multi-Mode Reader at excitation and emission wavelengths of 550 nm and 620 nm, respectively.

Binding assay *in vivo*. Cultured C8161 cells (10^6 cells per mouse in 0.1 mL saline) were subcutaneously injected into the back of NSG mice. The size of the tumor was measured twice each week using a digital Vernier caliper. Tumor volume was estimated by the following formula: volume= $(a \times b2) \times \pi/6$, where a and b are major and minor axes of the tumor. When the tumor reached 800 mm^3, FA ligand based, fluorescently labeled micelles were intravenously injected into mouse-tail vein. 72 h post i.v. injection, organs including blood and tumor were collected and analyzed through fluorescence with a NightOWL II device

ASSOCIATED CONTENT

Supporting Information

The Supporting Information is available free of charge.

Additional experimental data and explanation including: Synthesis of ABA amphiphilic triblock PMOXA-b-PDMS-b-PMOXA copolymers; Electrokinetic charge calculation for **E4** -Pipz-17 and **E1** -Pipz-7 based micelles; Self-assembly in aqueous solution: from polymer structure to micelle shape elucidated by computer modeling; Relationship between temperature and cellular uptake for polymers **J4**, **E1** and **H1** based micelles; Composition of the polymers investigated in the present study (Table S1); Calculated pKa for different terminal functional groups and their charge situations in aqueous solution (Table S2); Micelle size distribution diameter (DLS), Zeta potential (ζ) (Table S3); FL- fluorescence based CMC measurements, SAM- surface activity based measurements (Table S4); A cryo-TEM of polymer PMOXA-PDMS-PMOXA (Figure S1); Graph showing the hydrophilic strand protrusion from the hydrophobic shell and the charge of the outermost polymer residues for various polymer types (Figure S2); Mean residue ellipticity of HSA alone and in the presence of different polymeric micelles (Figure S3). **H1**, **J2**, and **E1** based micelle biodistribution in mice sacrificed after 24h, 1week, 1month, and 3 months, post i.v. injection, respectively (Figure S4).

AUTHOR INFORMATION

Corresponding Authors

Kegang Liu - Nanomedicine Research Lab. CLINAM, University of Basel, University Hospital Basel, Bernoullistrasse 20, CH-4056 Basel, Switzerland

Patrick Hunziker – Nanomedicine Research Lab. CLINAM, University of Basel, University Hospital Basel, Bernoullistrasse 20, CH-4056 Basel, Switzerland; Intensive Care Clinic, University Hospital Basel, Petersgraben 4, 4031 Basel, Switzerland; CLINAM Foundation for Nanomedicine, Alemannengasse, 4058 Basel, Switzerland

Authors

Xueya Wang- Nanomedicine Research Lab. CLINAM, University of Basel, University Hospital Basel, Bernoullistrasse 20, CH-4056 Basel, Switzerland

Xiaochun Li-Blatter-Biozentrum, University of Basel, Klingelbergstrasse 70, 4056 Basel,

Marc Wolf- Nanomedicine Research Lab. CLINAM, University of Basel, University Hospital Basel, Bernoullistrasse 20, CH-4056 Basel, Switzerland

Complete contact information is available at:

Author Contributions

K. Liu and X. Wang contributed equally to this work.

Notes

The authors declare no competing financial interest.

ACKNOWLEDGEMENTS

We acknowledge V. Oliveri and U. Sauder (Microscopy Center, University of Basel) for experimental support in carrying out the TEM measurements. We are grateful to Dr. T. Sharp for the technical help to perform the DLS (Biophysics Facility, University of Basel). Financial support of the Swiss National Science Foundation is gratefully acknowledged.

REFERENCES

1. Cooper, E. R. Nanoparticles: A personal experience for formulating poorly water soluble drugs. *J. Controlled Release* **2010,** *141*, 300-302.
2. Wais, U.; Jackson, A. W.; He, T.; Zhang, H. Nanoformulation and encapsulation approaches for poorly water-soluble drug nanoparticles. *Nanoscale* **2016,** *8*, 1746-69.
3. Maeda, H.; Nakamura, H.; Fang, J. The EPR effect for macromolecular drug delivery to solid tumors: Improvement of tumor uptake, lowering of systemic toxicity, and distinct tumor imaging in vivo. *Adv. Drug Delivery Rev.* **2013,** *65*, 71-79.
4. Lehner, R.; Wang, X.; Marsch, S.; Hunziker, P. Intelligent nanomaterials for medicine: carrier platforms and targeting strategies in the context of clinical application. *Nanomedicine* **2013,** *9*, 742-57.
5. Lee, J. H.; Huh, Y. M.; Jun, Y. W.; Seo, J. W.; Jang, J. T.; Song, H. T.; Kim, S.; Cho, E. J.; Yoon, H. G.; Suh, J. S.; Cheon, J. Artificially engineered magnetic nanoparticles for ultra-sensitive molecular imaging. *Nat. Med.* **2007,** *13*, 95-99.
6. Rwei, A. Y.; Wang, W.; Kohane, D. S. Photoresponsive nanoparticles for drug delivery. *Nano Today* **2015,** *10*, 451-467.
7. Lanza, G. M. Theranostic agents: From micro to nano in seconds. *Nat. Nanotechnol.* **2015,** *10*, 301-302.
8. Huber, M. C.; Schreiber, A.; von Olshausen, P.; Varga, B. R.; Kretz, O.; Joch, B.; Barnert, S.; Schubert, R.; Eimer, S.; Kele, P.; Schiller, S. M. Designer amphiphilic proteins as building blocks for the intracellular formation of organelle-like compartments. *Nat. Mater.* **2015,** *14*, 125-132.
9. Wagner, V.; Dullaart, A.; Bock, A.-K.; Zweck, A. The emerging nanomedicine landscape. *Nat. Biotechnol.* **2006,** *24*, 1211-1217.
10. Chen, Z. Small-molecule delivery by nanoparticles for anticancer therapy. *Trends. Mol. Med.* **2010**, *16*, 594-602.
11. Hubbell, J. A.; Langer, R. Translating materials design to the clinic. *Nat. Mater.* **2013,** *12*, 963-966.

12. Fleischer, C. C.; Payne, C. K. Secondary structure of corona proteins determines the cell surface receptors used by nanoparticles. *J. Phys. Chem. B* **2014,** *118*, 14017-26.
13. Liu, Y.; Zhong, R.; Zhang, P.; Ma, Y.; Yun, X.; Gong, P.; Wei, J.; Zhao, X.; Zhang, F. Understanding the Robust Physisorption between Bovine Serum Albumin and Amphiphilic Polymer Coated Nanoparticles. *ACS Appl. Mater. Interfaces* ***2016****, 8, 2478-2485.*
14. *M*affre, P.; Brandholt, S.; Nienhaus, K.; Shang, L.; Parak, W. J.; Nienhaus, G. U. Effects of surface functionalization on the adsorption of human serum albumin onto nanoparticles - a fluorescence correlation spectroscopy study. *Beilstein J. Nanotechnol.* **2014**, *5*, 2036-47.
15. del Pino, P.; Yang, F.; Pelaz, B.; Zhang, Q.; Kantner, K.; Hartmann, R.; Martinez de Baroja, N.; Gallego, M.; Möller, M.; Manshian, B. B.; Soenen, S. J.; Riedel, R.; Hampp, N.; Parak, W. J. Basic Physicochemical Properties of Polyethylene Glycol Coated Gold Nanoparticles that Determine Their Interaction with Cells. *Angew. Chem., Int. Ed.* **2016**, *55*, 5483-5487.
16. Pelaz, B.; del Pino, P.; Maffre, P.; Hartmann, R.; Gallego, M.; Rivera-Fernández, S.; de la Fuente, J. M.; Nienhaus, G. U.; Parak, W. J. Surface Functionalization of Nanoparticles with Polyethylene Glycol: Effects on Protein Adsorption and Cellular Uptake. *ACS Nano* **2015**, *9*, 6996-7008.
17. Shiraishi, K.; Kawano, K.; Maitani, Y.; Aoshi, T.; Ishii, K. J.; Sanada, Y.; Mochizuki, S.; Sakurai, K.; Yokoyama, M. Exploring the relationship between anti-PEG IgM behaviors and PEGylated nanoparticles and its significance for accelerated blood clearance. *J. Controlled Release* **2016**, *234*, 59-67.
18. Woo, J. R.; Lim, D. K.; Nam, J. M. Minimally stable nanoparticle-based colorimetric assay for simple, rapid, and sensitive antibody structure and activity evaluation. *Small* **2011**, *7*, 648-55.
19. Chen, H.; Wang, L.; Yeh, J.; Wu, X.; Cao, Z.; Wang, Y. A.; Zhang, M.; Yang, L.; Mao, H. Reducing non-specific binding and uptake of nanoparticles and improving cell targeting with an antifouling PEO-b-PγMPS copolymer coating. *Biomaterials* **2010**, *31*, 5397-5407.
20. Sun, T.; Zhang, Y. S.; Pang, B.; Hyun, D. C.; Yang, M.; Xia, Y. Engineered nanoparticles for drug delivery in cancer therapy. *Angew. Chem., Int. Ed.* **2014**, *53*, 12320-64.
21. Liu, R.; Kay, B. K.; Jiang, S.; Chen, S. Nanoparticle Delivery: Targeting and Nonspecific Binding. *MRS Bulletin* **2009**, *34*, 432-440.
22. Zhang, Z.; Ma, R.; Shi, L. Cooperative macromolecular self-assembly toward polymeric assemblies with multiple and bioactive functions. *Acc. Chem. Res.* **2014**, *47*, 1426-1437.
23. Loos, C.; Syrovets, T.; Musyanovych, A.; Mailander, V.; Landfester, K.; Nienhaus, G. U.; Simmet, T. Functionalized polystyrene nanoparticles as a platform for studying bio-nano interactions. *Beilstein J. Nanotechnol.* **2014**, *5*, 2403-2412.
24. Dong, H.; Shu, J. Y.; Dube, N.; Ma, Y.; Tirrell, M. V.; Downing, K. H.; Xu, T. 3-Helix micelles stabilized by polymer springs. *J. Am. Chem. Soc.* **2012**, *134*, 11807-11814.
25. LoPresti, C.; Massignani, M.; Fernyhough, C.; Blanazs, A.; Ryan, A. J.; Madsen, J.; Warren, N. J.; Armes, S. P.; Lewis, A. L.; Chirasatitsin, S.; Engler, A. J.; Battaglia, G. Controlling polymersome surface topology at the nanoscale by membrane confined polymer/polymer phase separation. *ACS nano* **2011**, *5*, 1775-1784.
26. Kazunori, K.; Glenn S, K.; Masayuki, Y.; Teruo, O.; Yasuhisa, S. Special Issue Proceedings of the Second European Symposium on Controlled Drug Delivery Block copolymer micelles as vehicles for drug delivery. *J. Controlled Release* **1993**, *24*, 119-132.
27. Szebeni, J. Hemocompatibility testing for nanomedicines and biologicals: predictive assays for complement mediated infusion reactions. *Eur. J. Nanomed.* **2012**, 4, 33-53.

28. Saadati, R.; Dadashzadeh, S.; Abbasian, Z.; Soleimanjahi, H. Accelerated blood clearance of PEGylated PLGA nanoparticles following repeated injections: effects of polymer dose, PEG coating, and encapsulated anticancer drug. *Pharm. Res.* **2013**, *30*, 985-995.
29. Matsumura, Y.; Maeda, H. A new concept for macromolecular therapeutics in cancer chemotherapy: mechanism of tumoritropic accumulation of proteins and the antitumor agent smancs. *Cancer Res.* **1986**, *46*, 6387-6392.
30. Silva, J. M.; Videira, M.; Gaspar, R.; Preat, V.; Florindo, H. F. Immune system targeting by biodegradable nanoparticles for cancer vaccines. *J. Controlled Release* **2013**, *168*, 179-199.
31. Frohlich, E. Action of Nanoparticles on Platelet Activation and Plasmatic Coagulation. *Curr. Med. Chem.* **2016**, *23*, 408-30.
32. Davis, M. E.; Chen, Z. G.; Shin, D. M. Nanoparticle therapeutics: an emerging treatment modality for cancer. *Nat. Rev. Drug Discov.* **2008**, *7*, 771-782.
33. Duncan, R. Polymer conjugates as anticancer nanomedicines. *Nat. Rev. Cancer* **2006**, *6*, 688-701.
34. Lammers, T.; Hennink, W. E.; Storm, G. Tumour-targeted nanomedicines: principles and practice. *Br. J. Cancer* **2008**, *99*, 392-397.
35. Nishiyama, N.; Kataoka, K. Current state, achievements, and future prospects of polymeric micelles as nanocarriers for drug and gene delivery. *Pharmacol. Therapeut.* **2006**, *112*, 630-648.
36. Torchilin, V. P. Recent advances with liposomes as pharmaceutical carriers. *Nat. Rev. Drug Discov.* **2005**, *4*, 145-160.
37. Peer, D.; Karp, J. M.; Hong, S.; Farokhzad, O. C.; Margalit, R.; Langer, R. Nanocarriers as an emerging platform for cancer therapy. *Nat. Nanotechnol.* **2007**, *2*, 751-760.
38. Ben-Haim, N.; Broz, P.; Marsch, S.; Meier, W.; Hunziker, P. Cell-specific integration of artificial organelles based on functionalized polymer vesicles. *Nano Lett.* **2008**, *8*, 1368-1373.
39. Egli, S.; Nussbaumer, M. G.; Balasubramanian, V.; Chami, M.; Bruns, N.; Palivan, C.; Meier, W. Biocompatible functionalization of polymersome surfaces: a new approach to surface immobilization and cell targeting using polymersomes. *J. Am. Chem. Soc.* **2011,** *133*, 4476-4483.
40. Konradi, R.; Pidhatika, B.; Muhlebach, A.; Textor, M. Poly-2-methyl-2-oxazoline: a peptide-like polymer for protein-repellent surfaces. *Langmuir* **2008**, *24*, 613-616.
41. Pidhatika, B.; Rodenstein, M.; Chen, Y.; Rakhmatullina, E.; Muhlebach, A.; Acikgoz, C.; Textor, M.; Konradi, R. Comparative stability studies of poly(2-methyl-2-oxazoline) and poly(ethylene glycol) brush coatings. *Biointerphases* **2012**, 7, https://doi.org/10.1007/s13758-011-0001-y.
42. Hoogenboom, R. Poly(2-oxazoline)s: a polymer class with numerous potential applications. *Angew. Chem., Int. Ed.* **2009**, *48*, 7978-7994.
43. Sedlacek, O.; Monnery, B. D.; Filippov, S. K.; Hoogenboom, R.; Hruby, M. Poly(2-oxazoline)s-are they more advantageous for biomedical applications than other polymers? *Macromol. Rapid Commun.* **2012**, *33*, 1648-1662.
44. Wolf, M. P.; Salieb-Beugelaar, G. B.; Hunziker, P. PDMS with designer functionalities-Properties, modifications strategies, and applications. *Prog. Polym. Sci.* **2018**, *83*, 97-134.
45. Liu, K.; Zhu, Z.; Wang, X.; Goncalves, D.; Zhang, B.; Hierlemann, A.; Hunziker, P. Microfluidics-based single-step preparation of injection-ready polymeric nanosystems for medical imaging and drug delivery. *Nanoscale* **2015**, *7*, 16983-16993.
46. Bernard, A. M. Molecular modeling of poly(2-ethyl-2-oxazoline). Ph.D. Thesis, Georgia Institute of Technology, 2008.

47. Mukose, T.; Fujiwara, T.; Nakano, J.; Taniguchi, I.; Miyamoto, M.; Kimura, Y.; Teraoka, I.; Woo Lee, C. Hydrogel formation between enantiomeric B-A-B-type block copolymers of polylactides (PLLA or PDLA: A) and polyoxyethylene (PEG: B); PEG-PLLA-PEG and PEG-PDLA-PEG. *Macromol. Biosci.* **2004**, *4*, 361-367.
48. Ramos, J.; Forcada, J.; Hidalgo-Alvarez, R. Cationic polymer nanoparticles and nanogels: from synthesis to biotechnological applications. *Chem. Rev.* **2014**, *114*, 367-428.
49. Pangon, A.; Tashiro, K.; Chirachanchai, S. Polyethylenimine containing benzimidazole branching: a model system providing a balance of hydrogen bond network or chain mobility enhances proton conductivity. *J. Phys. Chem. B.* **2011**, *115*, 11359-67.
50. Halgren, T. A. Merck molecular force field .1. Basis, form, scope, parameterization, and performance of MMFF94. *J. Comput. Chem.* 1**996**, *17*, 490-519.
51. Chithrani, B. D.; Ghazani, A. A.; Chan, W. C. Determining the size and shape dependence of gold nanoparticle uptake into mammalian cells. *Nano lett.* **2006**, *6*, 662-668.
52. Rejman, J.; Oberle, V.; Zuhorn, I. S.; Hoekstra, D. Size-dependent internalization of particles via the pathways of clathrin- and caveolae-mediated endocytosis. *Biochem. J.* **2004**, *377*, 159-169.
53. Labhasetwar, V.; Song, C.; Humphrey, W.; Shebuski, R.; Levy, R. J. Arterial uptake of biodegradable nanoparticles: effect of surface modifications. *J. Pharm. Sci.* **1998**, *87*, 1229-1234.
54. Sun, X.; Rossin, R.; Turner, J. L.; Becker, M. L.; Joralemon, M. J.; Welch, M. J.; Wooley, K. L. An assessment of the effects of shell cross-linked nanoparticle size, core composition, and surface PEGylation on in vivo biodistribution. *Biomacromolecules* **2005**, *6*, 2541-2554.
55. Nativo, P.; Prior, I. A.; Brust, M. Uptake and intracellular fate of surface-modified gold nanoparticles. *ACS nano* **2008**, *2*, 1639-1644.
56. McNeil, S. E. Challenges for nanoparticle characterization. *Methods Mol. Biol.* **2011**, *697*, 9-15.
57. Frohlich, E. The role of surface charge in cellular uptake and cytotoxicity of medical nanoparticles. *Int. J. Nanomed.* **2012**, *7*, 5577-91.
58. Amin, M. L.; Joo, J. Y.; Yi, D. K.; An, S. S. Surface modification and local orientations of surface molecules in nanotherapeutics. *J. Controlled Release* **2015**, *207*, 131-42.
59. Smith, G. N.; Eastoe, J. Controlling colloid charge in nonpolar liquids with surfactants. *Phys. Chem. Chem. Phys.* **2013**, *15*, 424-439.
60. Cho, E. J.; Holback, H.; Liu, K. C.; Abouelmagd, S. A.; Park, J.; Yeo, Y. Nanoparticle characterization: state of the art, challenges, and emerging technologies *Mol. Pharm.* **2013,** *10*, 2093-2110.
61. Duhr, S.; Braun, D. Why molecules move along a temperature gradient. *Proc. Natl. Acad. Sci. U.S.A.* **2006,** 103, 19678-19682.
62. Gerebtzoff, G.; Li-Blatter, X.; Fischer, H.; Frentzel, A.; Seelig, A. Halogenation of drugs enhances membrane binding and permeation. *Chembiochem* **2004**, 5, 676-84.
63. Yang, J. T.; Wu, C. S.; Martinez, H. M. Calculation of protein conformation from circular dichroism. *Methods Enzymol.* **1986**, *130*, 208-269.

Graphic Abstract: